Ligand-induced allostery in the interaction of the *Pseudomonas aeruginosa* heme binding protein with heme oxygenase

Daniel J. Deredge[a,1], Weiliang Huang[a,1], Colleen Hui[b], Hirotoshi Matsumura[b], Zhi Yue[a], Pierre Moënne-Loccoz[b], Jana Shen[a], Patrick L. Wintrode[a], and Angela Wilks[a,2]

[a]Department of Pharmaceutical Sciences, School of Pharmacy, University of Maryland, Baltimore, MD 21201; and [b]Institute of Environmental Health, Division of Environmental and Biomolecular Systems, Oregon Health and Science University, Portland, OR 97239

Edited by Brian M. Hoffman, Northwestern University, Evanston, IL, and approved February 13, 2017 (received for review May 2, 2016)

A heme-dependent conformational rearrangement of the C-terminal domain of heme binding protein (PhuS) is required for interaction with the iron-regulated heme oxygenase (HemO). Herein, we further investigate the underlying mechanism of this conformational rearrangement and its implications for heme transfer via site-directed mutagenesis, resonance Raman (RR), hydrogen–deuterium exchange MS (HDX-MS) methods, and molecular dynamics (MD). HDX-MS revealed that the apo-PhuS C-terminal α6/α7/α8-helices are largely unstructured, whereas the apo-PhuS H212R variant showed an increase in structure within these regions. The increased rate of heme association with apo-PhuS H212R compared with the WT and lack of a detectable five-coordinate high-spin (5cHS) heme intermediate are consistent with a more folded and less dynamic C-terminal domain. HDX-MS and MD of holo-PhuS indicate an overall reduction in molecular flexibility throughout the protein, with significant structural rearrangement and protection of the heme binding pocket. We observed slow cooperative unfolding/folding events within the C-terminal helices of holo-PhuS and the N-terminal α1/α2-helices that are dampened or eliminated in the holo-PhuS H212R variant. Chemical cross-linking and MALDI-TOF MS mapped these same regions to the PhuS:HemO protein–protein interface. We previously proposed that the protein–protein interaction induces conformational rearrangement, promoting a ligand switch from His-209 to His-212 and triggering heme release to HemO. The reduced conformational freedom of holo-PhuS H212R combined with the increase in entropy and decrease in heme transfer on interaction with HemO further support this model. This study provides significant insight into the role of protein dynamics in heme binding and release in bacterial heme transport proteins.

heme binding | allostery | protein–protein interaction | *Pseudomonas aeruginosa* | heme transfer

Iron is an essential micronutrient required for the survival and virulence of most bacterial pathogens. Furthermore, iron sequestration by the host's defense systems drives the diversity of iron acquisition mechanisms deployed by pathogens (1). To combat iron limitations, many pathogens use several iron acquisition strategies, including utilization of host heme-containing proteins (2). The opportunistic pathogen *Pseudomonas aeruginosa* encodes two distinct heme uptake systems: the *Pseudomonas* heme uptake (*phu*) and the heme assimilation system (*has*) (3). We have recently shown the Has and Phu systems perform nonredundant roles in the sensing and transport of heme, respectively (4). The Phu system comprises a TonB-dependent outer membrane receptor (PhuR) and a soluble heme binding protein (PhuT) that acts as the receptor for an ATP-dependent permease (ABC transporter), which then translocates heme to the cytoplasm. In the cytoplasm, the cytoplasmic heme binding protein (PhuS) sequesters and chaperones heme to the iron-regulated heme oxygenase (HemO) (5, 6). In the cytoplasm, heme is oxidatively cleaved by HemO to biliverdin IXδ (BVIXδ) and BVIXβ with the release of iron and CO (7). It was recently determined that the Phu system is the primary iron acquisition system in *P. aeruginosa* chronic infection of the cystic fibrosis lung and up-regulated coincident with a decrease in the levels of the major secreted siderophore pyoverdine (8, 9). This increase is in large part caused by point mutations within the promoter region of the *phu* operon leading to increased expression of PhuR (8). Therefore, understanding the molecular mechanisms by which *P. aeruginosa* acquires and uses heme may provide a therapeutic strategy in the treatment of *P. aeruginosa* chronic infections.

Previous studies from our laboratory have shown the interaction of PhuS with HemO is driven by a conformational change on ligand binding (6, 10). Furthermore, the previously reported kinetics of heme transfer from PhuS to HemO are slow: on the second timescale at 34 °C (11). Based on these data, we proposed that a His-ligand switch from His-209 to His-212 within holo-PhuS occurs before heme transfer to HemO. In this report, we further show that (*i*) heme binding to the C-terminal proximal α6/α7/α8-helices (residues 207–233) drives a conformational change required for protein–protein interaction, (*ii*) cooperative folding and unfolding events in the N- and C-terminal domains at the protein–protein interface trigger heme release to HemO, and (*iii*) these studies support a heme translocation pathway or "exit from the side" mechanism that requires a ligand switch from His-209 to His-212 before release of heme to HemO.

Significance

Heme is a critical source of iron for *Pseudomonas aeruginosa* on infection of the host. The flux of heme into the cell is driven by the catalytic action of heme oxygenase (HemO) and regulated by the heme binding protein (PhuS). Despite advances in structural characterization of bacterial heme uptake proteins, the mechanism of heme transfer is poorly defined. In this study, we determined structural elements within PhuS that undergo conformational rearrangement on heme binding and further show that allosteric linkage between the N- and C-terminal domains of PhuS is critical for triggering heme release to HemO. These studies provide a first step in defining the role of protein conformation and allosteric contributions in heme transfer within bacterial heme uptake systems.

Author contributions: D.J.D., W.H., P.M.-L., J.S., P.L.W., and A.W. designed research; D.J.D., W.H., C.H., H.M., Z.Y., and P.M.-L. performed research; D.J.D., W.H., C.H., H.M., Z.Y., P.M.-L., J.S., P.L.W., and A.W. analyzed data; and D.J.D., W.H., P.M.-L., J.S., P.L.W., and A.W. wrote the paper.

The authors declare no conflict of interest.

This article is a PNAS Direct Submission.

[1]D.J.D. and W.H. contributed equally to this work.

[2]To whom correspondence should be addressed. Email: awilks@rx.umaryland.edu.

This article contains supporting information online at www.pnas.org/lookup/suppl/doi:10.1073/pnas.1606931114/-/DCSupplemental.

Results

Conformational Rearrangement on Heme Binding to PhuS. Comparison of deuterium uptake between apo- and holo-PhuS was monitored after dilution into D_2O. Samples were removed at various time points, and the exchange was quenched. Regions of the protein that undergo extensive exchange at the earliest time points reflect regions that are exposed to solvent and intrinsically unstructured or regions undergoing rapid equilibrium favoring the unstructured form. In contrast, exchange times on the scale of minutes to hours are more indicative of the flexibility of the secondary and tertiary structures of the protein. The peptide fragments provided 99% coverage for both the WT and H212R PhuS apo and holo forms (Fig. S1). Global examination at all time points for deuterium exchange in apo- vs. holo-PhuS shows significant protection on heme binding, indicative of an overall decrease in the flexibility and dynamics of the protein (gray bars in Fig. 1*A*). The PhuS heme binding site is between the proximal C-terminal helices (α6/α7/α8), the distal N-terminal domain β-sheets (β5–β6), and β-sheets (β16/β17/β18) on the backside of the pocket (Fig. 1 *C* and *D*). Hydrogen–deuterium exchange MS (HDX-MS) methods and molecular dynamics (MD) studies comparing the apo and holo forms of WT PhuS point to structural and conformational effects of heme binding on these structural elements. HDX-MS reveals particularly strong losses in deuterium incorporation for all three structural motifs, including those that are involved in secondary structure in both the apo and holo crystal structures (Fig. 1*A*). Consistent with HDX-MS, MD shows a decrease in fluctuation of two of these three structural motifs in the holo form as evidenced by the decrease in the rms fluctuation (Fig. 1*B*). In particular, the loop regions between the C-terminal helices α6 and α7, between the β-sheets β16 and β17, and between β18 and α10 on the backside of the pocket show the greatest loss in fluctuations. The lack of difference in fluctuation in the helices and β-sheets of these motifs can be attributed to the significantly shorter simulation timescale (500 ns) compared with that of HDX-MS and the limitation of the current force field (energy function) that tends to overstabilize secondary structure elements. Additionally, in contrast to HDX-MS, the MD data suggest that the third structural motifs, the distal N-terminal domain β-sheets (β5–β6), are not affected by heme binding. Additional analysis of the extent of deuteration over time for β-sheets β5 and β6 reveals comparable levels of protection in the early time points for both apo- and holo-PhuS (Fig. S2). However, EX1 kinetics are observed within the first 10 min in apo-PhuS and are clearly slowed in holo-PhuS (~1 h), indicating an increased stability in these secondary structures on ligand binding (Fig. S2). Such kinetics are usually indicative of slow conformational changes that are outside of the timescale probed by MD. In the crystal structure of holo-PhuS, Leu-103 and Phe-114 of the β-sheets (β5–β6) engage in nonpolar contacts with the heme, whereas Arg-112 is hydrogen-bonded through its guanidinium group to a distal solvent molecule coordinated to the heme iron (Fig. 1*D*) (12). Interestingly, although secondary structures remained stable in MD simulations of apo- and holo-PhuS, the heme binding cleft of apo-PhuS exhibited significant breathing motion, whereas it remained closed in holo-PhuS. To characterize the binding cleft dynamics, the free energy surface with respect to the radius of gyration of the heme binding cleft (R_g) and the Cα distance between Arg-112 and His-209 ($D_{R112\text{-}H209}$) was calculated from the MD trajectories (Fig. S3). R_g represents the volume of the binding cleft, and Arg-112 and His-209 are two conserved residues above and below the heme, respectively. Remarkably, the free energy minimum for apo-PhuS is located at R_g of 15.4 Å and $D_{R112\text{-}H209}$ of 15 Å, whereas the minimum for holo-PhuS remains at the position close to the crystal structure (R_g of 14.5 Å and $D_{R112\text{-}H209}$ of 11 Å). These data indicate that heme binding rigidifies the initially open and flexible binding cleft to adopt the closed conformation seen in the crystal structure. In solution, the full extent of opening and flexibility of the binding cleft in apo-PhuS is further revealed by a more detailed analysis of the HDX-MS. At the earliest time point probed (10 s), peptides comprising the C-terminal proximal helices α6/α7/α8 display deuterium exchange levels greater than 50% (>80% within 1 min), indicating that the proximal heme binding helices are largely unstructured (solid lines in Fig. 2 *A*, *Upper* and *B*, *Upper*). On heme binding, significant protection within the C-terminal helices is observed within 10 s, indicating that heme binding drives a large structural and conformational rearrangement of the C-terminal domain (dashed red lines in Fig. 2 *A*, *Upper* and *B*, *Upper*). These data are consistent with previous solution studies showing that heme binding shifts the sedimentation coefficient distribution for holo-PhuS and

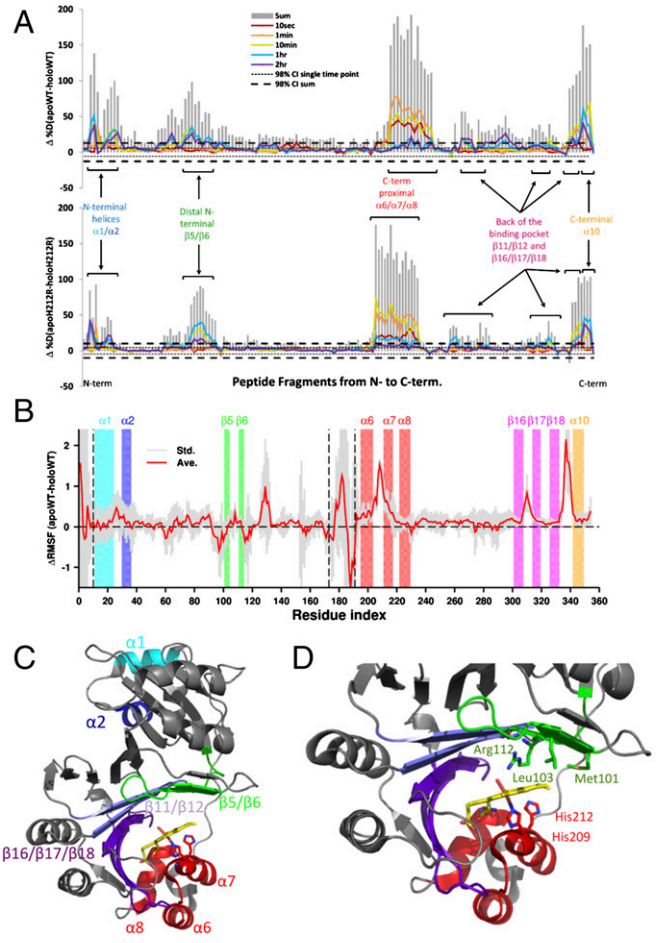

Fig. 1. (*A*) Difference plot of percentage deuteration (Δ%*D*) apo- minus holo-PhuS for (*Upper*) the WT and (*Lower*) H212R mutant. Individual peptides are plotted on the *x* axis from N to C terminus based on the first residue number. For each peptide, differences in percentage deuteration at the various deuterium incubation times are color-coded according to the legend, and the sums of all differences integrated over all incubation time points are represented in gray bars. Respective 98% confidence intervals (98% CIs) are represented as horizontal dashed lines. (*B*) Differences in C_α atom rms fluctuations (ΔRMSFs) between WT apo and holo simulations (solid red curve) plotted along the protein sequence. Positive values indicate increased rigidity on heme binding. Shaded gray area indicates statistical uncertainty. The regions that exhibit the most significant changes in deuterium uptake in *A* are marked by color-coded boxes. Vertical dashed black lines highlight the loops. (*C*) Regions displaying the most significant changes in deuterium uptake have been labeled in color and mapped onto the crystal structure of holo-PhuS (PDB ID code 4MF9). (*D*) Binding site of holo-PhuS with key residues shown in stick format. Structural domains are colored as in *A* and *B*.

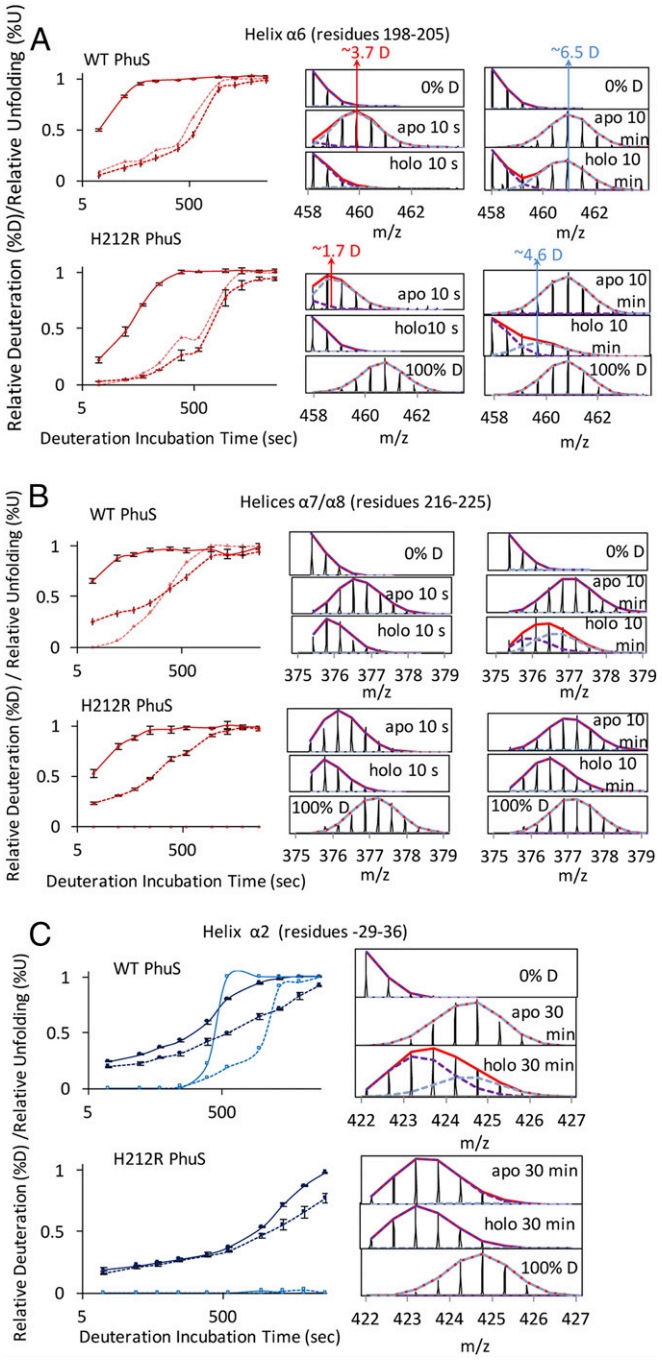

Fig. 2. HDX-MS reveals heme-induced effects on conformational dynamics of WT and H212R PhuS. Deuterium kinetic traces for the C-terminal (*A*) α6-helix and (*B*) α7/α8-helices and (*C*) N-terminal α2-helix are color-coded as in Fig. 1*C*. In *A* and *B*, the traces are as follows: %*D* apo (solid line; dark red), %*D* holo (dashed line; dark red), and %*U* holo (dashed line; pink), and in *C*, the traces are as follows: %*D* apo (solid line; dark blue), %*U* apo (solid line; light blue), %*D* holo (dashed line; dark blue), and %*U* holo (dashed line; light blue). Kinetic traces include the percentage deuteration (%*D*) and the percentage unfolded (%*U*) as a function of deuterium incubation time; %*D* is determined as the centroid of the isotopic envelope normalized to undeuterated and fully deuterated controls. Stacked mass spectra at 10 s and 10 min for peptides 198–205 (*A*) and 216–225 (*B*), and 30 min for peptide 29–26 (*C*) displaying instances of double-isotopic envelopes typical of EX1 kinetics are shown in *Right*. %*U* represents the relative proportion of the unprotected envelope (light blue dashed distribution) as a function of deuterium incubation time as determined by HX-express2.

further protects the C-terminal domain from proteolysis (10). Interestingly, the HDX-MS data are not consistent with the recent apo-PhuS crystal structures, where the overall structural fold is almost identical to that of holo-PhuS, suggesting that the apo-PhuS crystal structures are more representative of the ligand-bound state (12, 13). The latter is supported by MD-based calculations of deuterium uptake. Indeed, for all peptides spanning the C-terminal helices, the calculated deuterium uptakes of apo and holo forms are identical and display uptake traces that are largely similar to the experimental deuterium uptake curves of the holo-PhuS (Fig. S4). Taken together, the MD and HDX-MS data support our previous "induced fit" hypothesis that heme binding drives conformational rearrangement of the C-terminal domain and subsequent ligand coordination.

Allosteric Contributions to Holo-PhuS Interaction with HemO. Insight into the dynamic flexibility of the heme binding pocket can be gained from the differences in deuterium exchange profiles in the presence and absence of the ligand. The slower EX1 unfolding kinetics in the distal β5/β6-sheets on heme binding reveal increased rigidity within this region compared with the apo-PhuS, whereas the C-terminal proximal α6/α7/α8 helices, after initial structural rearrangement, undergo cooperative unfolding characterized by the EX1 double-isotopic envelope beyond the 5-min time point (dashed pink lines in Fig. 2 *A*, *Upper* and *B*, *Upper*). A similar rate of unfolding in the α1/α2-helices (dashed light blue lines in Fig. 2*C*, *Upper*) of the N-terminal domain distant from the heme binding pocket is consistent with long-range allosteric effects.

Based on the previously calculated slow rate of heme transfer from PhuS to HemO (0.1 s^{-1}), it is reasonable to suggest the cooperative folding/unfolding motions may contribute to a His ligand switch from His-209 to His-212 that triggers heme release to HemO (11). Interestingly, the PhuS:HemO formaldehyde cross-linked complex detected by Western blot (Fig. S5) when subjected to tryptic digest and MALDI-TOF analysis revealed peptides within PhuS shown to undergo EX1 kinetics in the HDX-MS experiments. PhuS peptides 217–222, 218–222, and 223–227 from the C-terminal α7/α8-helices cross-link distal helix residues 124–132 and 133–145 of HemO, and PhuS peptides 228–236 and 296–304 from the β10- and β15-sheets flanking the binding pocket cross-link to proximal helix residues 35–42 of HemO (Fig. 3*A*). Furthermore, the PhuS N-terminal α1/α2-helices that are cooperatively linked to the motions of the C-terminal domain also map to the PhuS:HemO interface. The complete set of peptides from the in-gel tryptic digest of the formaldehyde-treated PhuS:HemO is listed in Table S1.

Increased Structural Rigidity in the PhuS H212R Mutant Inhibits Heme Release to HemO. The role of the conformational dynamics and long-range coupling of the C-terminal α6/α7/α8-helices with the N-terminal α1/α2-helices is further supported in the PhuS H212R variant, which is impaired in its ability to release heme to HemO as judged by the heme distribution after separation of holo-PhuS and apo-HemO by size exclusion chromatography (Fig. S6). Isothermal titration calorimetry (ITC) analysis of the interaction of holo-PhuS H212R with HemO revealed an association constant $K_a = 6.3 \times 10^6$ M^{-1} and overall free energy of binding $\Delta G = -9.3$ kcal mol^{-1} (Fig. 3*C*); these values are similar to those previously reported for holo-PhuS WT ($K_a = 2.3 \times 10^6$ M^{-1}; $\Delta G = -8.3$ kcal mol^{-1}) (10). As for WT holo-PhuS, the interaction of H212R holo-PhuS with HemO is largely driven by enthalpic contributions; however, the moderate increase in entropy (~3 kcal mol^{-1}) suggests an increase in hydrophobic contributions and decreased conformational flexibility. The electronic absorption and resonance Raman (RR) spectra of holo-PhuS H212R reveal a heme coordination geometry that closely matches that of WT holo-PhuS (Fig. S7). The Soret absorption maximum of holo-PhuS H212R is observed at 412 nm, which corresponds to a 3-nm redshift compared with the Soret absorption

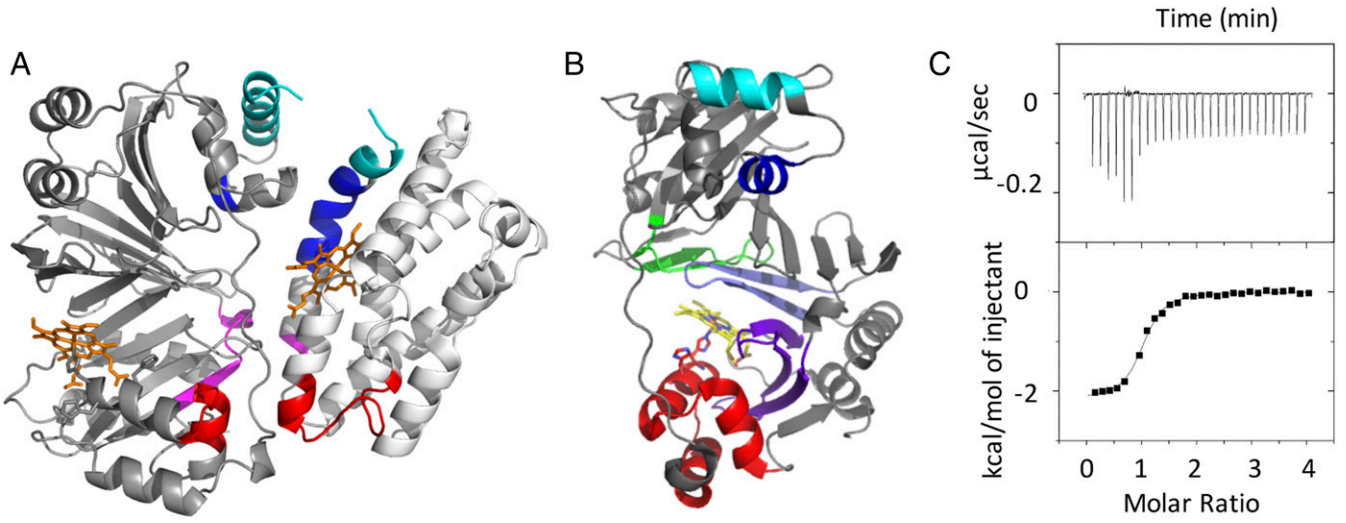

Fig. 3. Holo-PhuS H212R–HemO protein interaction. (*A*) The protein–protein interface as mapped by formaldehyde cross-linking and MALDI-TOF analysis. Cross-linking and MALDI-TOF analysis were performed as described in *Experimental Procedures*. Peptides identified at the protein interface that undergo EX1 kinetics in PhuS are color-coded as in Fig. 2. (*B*) Holo-PhuS structure displaying the proposed exit from the side pathway of heme release. His-209 (heme-bound) and His-212 are shown in stick form, and the regions displaying the most significant changes in deuterium uptake are color-coded as in Fig. 1. (*C*) ITC analysis of the holo-PhuS H212R interaction with apo-HemO. Titrations were performed in 20 mM sodium phosphate (pH 7.5) at 298 K. (*Upper*) Time-dependent release of heat during the titration. (*Lower*) Peak integrals as a function of the molar ratio of holo-PhuS to HemO. The data were fit to a single-site binding model with Origin software supplied by MicroCal Inc.

of WT holo-PhuS (Fig. S7*A*), and in the Q bands, visible bands at 542 and 580 nm are slightly more intense in H212R, suggesting a marginal increase in the low-spin (LS) to high-spin (HS) heme conformer ratio in H212R relative to the WT protein. This interpretation of the ultraviolet-visible (UV-vis) absorption spectra is supported by the high-frequency RR spectra of H212R holo-PhuS, which are almost identical to that of the WT with porphyrin skeletal modes ν_3, ν_2, and ν_{10}, indicative of a six-coordinate high-spin (6cHS)/six-coordinate low-spin (6cLS) equilibrium mixture, and a minor gain in relative intensity of the LS modes in the RR spectra of H212R (Fig. S7*B*). The vinyl stretching modes at 1,620 and 1,628 cm^{-1} are well-defined and unchanged by the H212R mutation (Fig. S7*B*).

Analysis of the apo- and holo-PhuS H212R proteins by HDX-MS revealed a significant decrease in the rate of deuterium exchange within the regions previously shown to undergo cooperative folding/unfolding in WT PhuS. Specifically, the α6- and α7/α8-helices of the C-terminal domain that appear largely unstructured in the apo-PhuS WT at the earliest 10-s time point show 30 and 10% less deuterium exchange at the same time point in apo-PhuS H212R, respectively (Fig. 2 *A* and *B*). Furthermore, distinct EX1 kinetics at the C-terminal α6-helix (peptides 198–205) are reduced in holo-PhuS H212R relative to the WT protein (dashed pink lines in Fig. 2*A*, *Lower*) and completely suppressed in the α7/α8-helices of holo-PhuS H212R (dashed pink lines in Fig. 2*B*, *Lower*). Surprisingly, the H212R substitution also decreased the conformational flexibility observed at the N-terminal α1/α2-helices in the WT protein, with a complete loss of the EX1 kinetics in the α2-helix as observed for the α7/α8-helices (light blue lines in Fig. 2*C*, *Lower*). The suppression of the cooperative unfolding events in both the N- and C-terminal domains suggests that these motions are allosterically coupled in a heme-dependent manner.

In keeping with a more structured C-terminal domain in apo-PhuS H212R, monitoring the process of heme binding to PhuS by stopped flow UV-vis spectroscopy at 4 °C revealed a significantly faster rate of heme binding to apo-PhuS H212R compared with the WT protein. Specifically, mixing hemin with apo-PhuS WT shows a gradual transition over 20 s from the spectrum of free hemin to that of holo-PhuS (Fig. 4*A*), whereas the first trace obtained after 4 ms with H212R apo-PhuS already shows a Soret maximum at 401 nm (Fig. 4*B*). Single-wavelength and global analyses of these kinetic data show triphasic processes for both proteins, with a first rate k_{obs1} with hyperbolic dependency on the apo-PhuS concentration and two slower phases, k_{obs2} and k_{obs3}, unaffected by the apoprotein concentration (Fig. 4 *C* and *D*). As with previous studies (14, 15), the hyperbolic dependence of k_{obs1} can be modeled by a two-step process that includes the formation of a hemin–apoprotein reversible complex followed by an iron (III) coordination step:

$$\text{apoprotein} + \text{hemin} \underset{k_{-1}}{\overset{k_1}{\rightleftharpoons}} \text{apoprotein} \cdot \text{hemin} \underset{k_{-hemin}}{\overset{k_{1coord}}{\rightleftharpoons}} \text{protein-bound hemin},$$

where $k_{obs1} = k_{1coord}$ [apoprotein]/(($k_{-1} + k_{1coord}$)/k_1 + [apoprotein]) ~ k_{1coord} [apoprotein]/K_d + [apoprotein] assuming k_1[apoprotein] and $k_{-1} >> k_{1coord} >> k_{-hemin}$.

We favor this model over that of a conformational rearrangement of apo-PhuS before heme binding based on the amphiphilic character of hemin that promotes rapid interaction with apoproteins, making a noninteracting apoconformer unlikely. Using this model with WT and H212R apo-PhuS leads to higher k_{1coord} and K_d values and an overall increase in hemin association rates in the H212R variant. The rapid freeze quench (RFQ)-RR analysis of hemin binding to WT and H212R apo-PhuS further supports the stopped flow kinetics, showing the establishment of the proximal His-coordinated spectrum within the earliest RFQ time of 9 ms with the H212R mutant (Fig. 4*E*). In contrast, the 9-ms RFQ-RR spectrum for the WT protein shows evidence of a five-coordinate HS heme conformer with porphyrin modes ν_3 and ν_2 at 1,492 and 1,561 cm^{-1}, respectively.

Overall, the higher K_d for the initial apoprotein•hemin complex but faster coordination steps in H212R relative to the WT protein are consistent with an initial apoprotein•hemin complex formation driven by noncoordinating π-stacking and hydrophobic interactions between the porphyrin and distal face β-sheets, triggering conformational rearrangement of the C-terminal domain and His-209 coordination to the heme iron. Increased folding of

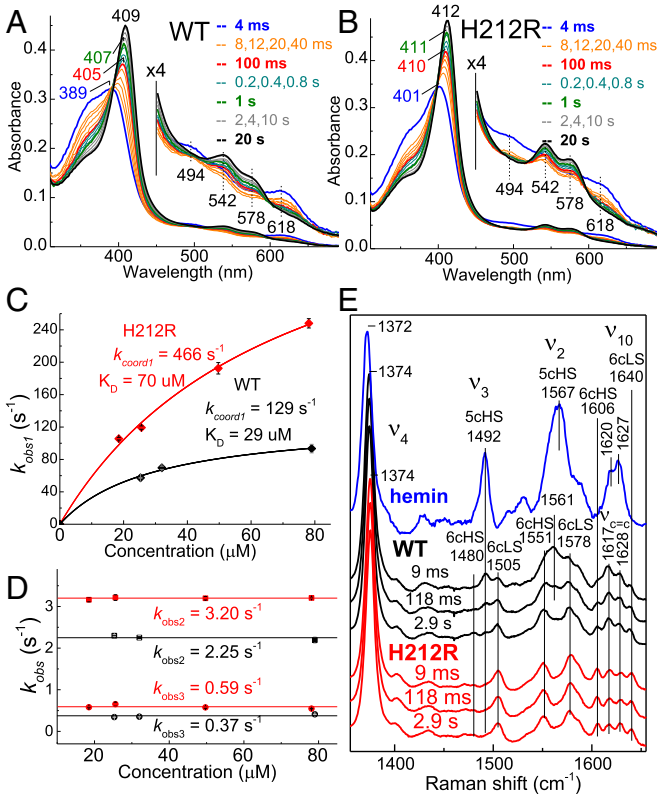

Fig. 4. Stopped flow absorption and RFQ-RR analysis of hemin binding to WT and H212R apo-PhuS. Stopped flow absorption spectra of the association of 3.5 μM hemin with ~25 μM (*A*) WT or (*B*) H212R apo-PhuS at 4 °C. (*C* and *D*) Plots of observed rate constants vs. apoprotein concentrations. (*E*) RR spectra of RFQ samples of the reaction of 1 eq hemin with ~150 μM WT (black), ~150 μM apo-PhuS (red), and buffer control (blue).

the C-terminal helices in apo-PhuS H212R may destabilize the apoprotein•hemin complex, while at the same time, prearrange H209 for heme iron coordination. The relatively slow first-order rates k_2 and k_3 revealed in the stopped flow traces would have been anticipated to result in different RR spectra for early RFQ samples relative to samples frozen a few seconds after mixing, but the RR spectra of H212R at 9 ms, 118 ms, and 2.9 s are nearly indistinguishable. This apparent discrepancy between stopped flow and RFQ data for H212R may reflect the impact of cryogenic temperatures on spin-state equilibrium in six-coordinate heme complexes with His/aqua axial ligands. Indeed, changing interactions between the heme iron (III) aqua ligand and residues lining the heme binding pocket can affect the HS to LS equilibrium ratio observed in the stopped flow measurements preformed at 4 °C but are unobserved in the RFQ-RR measurements performed at 110 K, because cryogenic temperatures depopulate the 6cHS species in favor of 6cLS conformers.

A Model for Heme Transfer. Based on the cross-linking data, a model of the docked holo-PhuS:HemO complex was obtained by in silico methods (Fig. 3*A*). In this docking orientation, heme must be translocated over 20 Å from PhuS to the heme binding site of HemO. Based on previous crystallographic data, we proposed a ligand switch from His-209 to His-212, with His-212 adopting an alternate rotamer, placing the heme in a more solvent-exposed region of the pocket where Arg-222 and Lys-216 are in a position to interact with the heme propionates (13). This positioning of the heme is consistent with the cross-linking data and provides a path for translocation of heme to HemO. The alternate rotamer adopted through heme coordination on His-212 orients the heme propionates at the protein–protein interface in close proximity to Lys-132 of HemO. Interaction of the heme propionate with Lys-132 of HemO may aid in facilitating transfer from PhuS to HemO. Interestingly, Lys-132 is required for stabilizing heme in the HemO active site in an orientation selective for β/δ-oxidative cleavage (16). These HDX-MS studies are consistent with this model, whereby the conformational flexibility at the dimer interface coupled with the allosteric modulation between the N- and C-terminal domains provides the free energy to trigger the His switch, opening up a path for heme translocation to HemO via an exit from the side mechanism (Fig. 3*B*). The decrease in conformational flexibility at the protein interface and resulting increase in entropy on holo-PhuS H212 interaction with HemO correlate with the inability to transfer heme to HemO.

Conclusions

We previously showed by sedimentation and limited proteolysis that, on heme binding, a conformational rearrangement of the PhuS C-terminal domain was required for interaction with HemO (10). Furthermore, site-directed mutagenesis and spectroscopic studies showed that either His-209 or His-212 could provide the proximal ligand to the heme (5). This study combining HDX-MS, MD, and stopped flow/RFQ-RR spectroscopic studies has provided additional insight into the role of the conformational flexibility of PhuS in driving heme transfer to HemO. HDX-MS analysis of apo-PhuS indicates that the C-terminal domain is largely unstructured, consistent with earlier proteolysis studies. Interestingly, deuterium uptake calculated from MD simulations based on the crystal structures of apo- and holo-PhuS are similar and for the apo form, deviate significantly from the experimental data, suggesting that the apo-PhuS crystal structure is along the trajectory of the more structured holo-PhuS. We propose that the conformational rearrangement and dynamics of the C-terminal domain of PhuS on heme binding drive both the ligand switch and protein–protein interaction with HemO (Fig. 5). Previous studies showed that the holo-PhuS H209A variant (where heme is coordinated through His-212) interacts and transfers heme to HemO. However, in contrast, the holo-PhuS H212R variant, while retaining the ability to interact with HemO, was unable to transfer heme to HemO. Thus, in our model, holo-PhuS conformers coordinated through either His-209 or His-212 are competent to interact with HemO; however, the heme ligand switch from His-209 to His-212 is required for heme transfer (Fig. 5). Furthermore, the overall decrease in conformational flexibility of the apo-PhuS H212R that increased the rate of heme binding but decreased cooperative folding and unfolding within regions at the protein interface highlights the critical role of allostery between the N- and C-terminal domains of PhuS in driving the heme ligand switch. The increase in entropic contributions on binding HemO as a result of the decreased conformational flexibility provides additional support for a model where the conformational flexibility and free energy on protein interaction drive heme translocation to HemO. Detailed spectroscopic studies are underway to further investigate the heme-ligated intermediates along the heme translocation pathway from holo-PhuS to HemO.

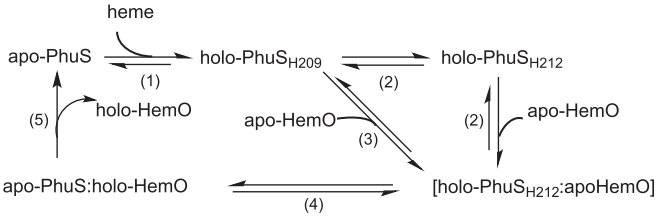

Fig. 5. Proposed mechanism for heme transfer from holo-PhuS to apo-HemO.

Experimental Procedures

Protein Expression and Purification. All bacterial strains and plasmids used in these studies were as previously reported (5, 6). Site-directed mutagenesis to create the PhuS H212R variant together with protein purification of WT PhuS, H212R PhuS, and HemO were carried out as previously described (5–7). A more detailed description is provided in *SI Experimental Procedures*.

HDX-MS. Liquid chromatography/MS workflow, coverage map and deuterium uptake determination, and deconvolution of biomodal isotopic envelops characteristic of EX1 kinetics were performed as described previously (17). A detailed description is provided in *SI Experimental Procedures*.

MD Simulations. Based on the crystal structures of the apo [Protein Data Bank (PDB) ID code 4IMH] (13) and holo (PDB ID code 4MF9) (12) PhuS, hybrid solvent continuous constant pH MD simulations with pH replica exchange protocol (18) were carried out using the CHARMM package (version c37b1) (19). To compare with the HDX-MS experiments, the deuterium uptake traces were calculated using protocols described by Radou et al. (20). Details of the simulation protocol and HDX-MS calculations are given in *SI Experimental Procedures*.

Cross-Linking and in Silico Modeling of the PhuS:HemO Complex. Holo-PhuS (50 μM) was mixed with an equimolar ratio of apo-HemO in 50 mM sodium phosphate buffer (pH 7.4), and the cross-linking reactions were initialized with a final concentration of 0.2% formaldehyde. The PhuS:HemO complex was modeled by using Cluspro 2.0 (21). Crystal structures of PhuS (PDB ID codes 4MF9 and 4IMH) and HemO (PDB ID code 1SK7) were used as template structures. A detailed description of the tryptic digest, peptide purification, and in silico modeling is provided in *SI Experimental Procedures*.

ITC. Titrations of apo-HemO with holo-PhuS WT and H212R were performed on a MicroCal MCS Titration Calorimeter (MicroCal Inc.) as previously described (10). A detailed description is provided in *SI Experimental Procedures*.

RR Spectroscopy. A custom McPherson 2061/207 spectrograph was used to obtain RR spectra. The spectrograph was equipped with a Princeton Instruments liquid N_2-cooled CCD detector (LN-1100PB). A Krypton laser (Innova 302; Coherent) was used to provide excitation at 407 nm.

Stopped Flow UV-Vis Spectroscopy. The apoprotein at varying concentrations in 200 mM Hepes (pH 7) and the hemin solution at 3.5 μM in 10 mM NaOH were loaded into an SX20 stopped flow UV-vis spectrometer (Applied Photophysics) and equilibrated to 4 °C. Excess solutions from each syringe were recovered from the apparatus after each experiment to confirm the concentrations of hemin and apoprotein by UV-vis spectroscopy; 1:1 mixtures of the hemin solution with Hepes buffer confirmed that the UV-vis spectrum of hemin alone was unchanged during the stopped flow experiments. RFQ samples after mixing of apo-PhuS with hemin were collected and analyzed by RR. A detailed description of the stopped flow experiments and RFQ methods is provided in *SI Experimental Procedures*.

ACKNOWLEDGMENTS. This work was supported by NIH Grant AI102833 (to A.W.) and in part by University of Maryland Baltimore School of Pharmacy Mass Spectrometry Center Grant SOP1841-IQB2014.

1. Collins HL (2008) Withholding iron as a cellular defence mechanism–friend or foe? *Eur J Immunol* 38(7):1803–1806.
2. Wilks A, O'Neill MJ (2014) Extracellular heme uptake and metabolism in bacterial pathogenesis. *Handbook of Porphyrin Science*, Heme Biochemistry, ed Ferreira GC (World Scientific, Singapore), 1st Ed, Vol 26, pp 268–306.
3. Ochsner UA, Johnson Z, Vasil ML (2000) Genetics and regulation of two distinct haem-uptake systems, *phu* and *has*, in *Pseudomonas aeruginosa*. *Microbiology* 146(Pt 1): 185–198.
4. Smith AD, Wilks A (2015) Differential contributions of the outer membrane receptors PhuR and HasR to heme acquisition in *Pseudomonas aeruginosa*. *J Biol Chem* 290(12):7756–7766.
5. Block DR, et al. (2007) Identification of two heme-binding sites in the cytoplasmic heme-trafficking protein PhuS from *Pseudomonas aeruginosa* and their relevance to function. *Biochemistry* 46(50):14391–14402.
6. Lansky IB, et al. (2006) The cytoplasmic heme-binding protein (PhuS) from the heme uptake system of *Pseudomonas aeruginosa* is an intracellular heme-trafficking protein to the delta-regioselective heme oxygenase. *J Biol Chem* 281(19):13652–13662.
7. Ratliff M, Zhu W, Deshmukh R, Wilks A, Stojiljkovic I (2001) Homologues of neisserial heme oxygenase in gram-negative bacteria: Degradation of heme by the product of the *pigA* gene of *Pseudomonas aeruginosa*. *J Bacteriol* 183(21):6394–6403.
8. Marvig RL, et al. (2014) Within-host evolution of *Pseudomonas aeruginosa* reveals adaptation toward iron acquisition from hemoglobin. *MBio* 5(3):e00966–e14.
9. Nguyen AT, et al. (2014) Adaptation of iron homeostasis pathways by a *Pseudomonas aeruginosa* pyoverdine mutant in the cystic fibrosis lung. *J Bacteriol* 196(12):2265–2276.
10. O'Neill MJ, Bhakta MN, Fleming KG, Wilks A (2012) Induced fit on heme binding to the *Pseudomonas aeruginosa* cytoplasmic protein (PhuS) drives interaction with heme oxygenase (HemO). *Proc Natl Acad Sci USA* 109(15):5639–5644.
11. Bhakta MN, Wilks A (2006) The mechanism of heme transfer from the cytoplasmic heme binding protein PhuS to the delta-regioselective heme oxygenase of *Pseudomonas aeruginosa*. *Biochemistry* 45(38):11642–11649.
12. Lee MJ, Schep D, McLaughlin B, Kaufmann M, Jia Z (2014) Structural analysis and identification of PhuS as a heme-degrading enzyme from *Pseudomonas aeruginosa*. *J Mol Biol* 426(9):1936–1946.
13. Tripathi S, O'Neill MJ, Wilks A, Poulos TL (2013) Crystal structure of the *Pseudomonas aeruginosa* cytoplasmic heme binding protein, Apo-PhuS. *J Inorg Biochem* 128:131–136.
14. Kumar R, et al. (2014) Replacing the axial ligand tyrosine 75 or its hydrogen bond partner histidine 83 minimally affects hemin acquisition by the hemophore HasAp from *Pseudomonas aeruginosa*. *Biochemistry* 53(13):2112–2125.
15. Yukl ET, et al. (2010) Kinetic and spectroscopic studies of hemin acquisition in the hemophore HasAp from *Pseudomonas aeruginosa*. *Biochemistry* 49(31):6646–6654.
16. Friedman J, Lad L, Li H, Wilks A, Poulos TL (2004) Structural basis for novel delta-regioselective heme oxygenation in the opportunistic pathogen *Pseudomonas aeruginosa*. *Biochemistry* 43(18):5239–5245.
17. Deredge D, Li J, Johnson KA, Wintrode PL (2016) Hydrogen/deuterium exchange kinetics demonstrate long range allosteric effects of thumb site 2 inhibitors of hepatitis C viral RNA-dependent RNA polymerase. *J Biol Chem* 291(19):10078–10088.
18. Wallace JA, Shen JK (2011) Continuous constant pH molecular dynamics in explicit solvent with pH-based replica exchange. *J Chem Theory Comput* 7(8):2617–2629.
19. Brooks BR, et al. (2009) CHARMM: The biomolecular simulation program. *J Comput Chem* 30(10):1545–1614.
20. Radou G, Dreyer FN, Tuma R, Paci E (2014) Functional dynamics of hexameric helicase probed by hydrogen exchange and simulation. *Biophys J* 107(4):983–990.
21. Comeau SR, Gatchell DW, Vajda S, Camacho CJ (2004) ClusPro: A fully automated algorithm for protein-protein docking. *Nucleic Acids Res* 32(Web Server issue):W96–W99.
22. Fuhrop JH, Smith KM, eds (1975) *Porphyrins and Metalloporhyrins* (Elsevier, Amsterdam), pp 804–807.
23. Houde D, Berkowitz SA, Engen JR (2011) The utility of hydrogen/deuterium exchange mass spectrometry in biopharmaceutical comparability studies. *J Pharm Sci* 100(6):2071–2086.
24. Guttman M, Weis DD, Engen JR, Lee KK (2013) Analysis of overlapped and noisy hydrogen/deuterium exchange mass spectra. *J Am Soc Mass Spectrom* 24(12):1906–1912.
25. Fiser A, Do RKG, Šali A (2000) Modeling of loops in protein structures. *Protein Sci* 9(9): 1753–1773.
26. Khandogin J, Brooks CL 3rd (2005) Constant pH molecular dynamics with proton tautomerism. *Biophys J* 89(1):141–157.
27. Im W, Lee MS, Brooks CL 3rd (2003) Generalized born model with a simple smoothing function. *J Comput Chem* 24(14):1691–1702.
28. Ellis CR, Shen J (2015) pH-dependent population shift regulates BACE1 activity and inhibition. *J Am Chem Soc* 137(30):9543–9546.
29. Mackerell AD Jr, Feig M, Brooks CL 3rd (2004) Extending the treatment of backbone energetics in protein force fields: Limitations of gas-phase quantum mechanics in reproducing protein conformational distributions in molecular dynamics simulations. *J Comput Chem* 25(11):1400–1415.
30. Hoover WG (1985) Canonical dynamics: Equilibrium phase-space distributions. *Phys Rev A Gen Phys* 31(3):1695–1697.
31. Feller SE, Zhang Y, Pastor RW, Brook BR (1995) Constant pressure molecular dynamics simulation: The Langevin piston method. *J Chem Phys* 103:4613–4621.
32. Essmann U, et al. (1995) A smooth particle mesh Ewald method. *J Chem Phys* 103: 8577–8593.
33. Ryckaert JP, Ciccotti G, Berendsen HJC (1977) Numerical integration of the cartesian equations of motion of a system with constraints: Molecular dynamics of n-alkanes. *J Comput Phys* 23:327–341.
34. Chen J, Im W, Brooks CL, 3rd (2006) Balancing solvation and intramolecular interactions: Toward a consistent generalized Born force field. *J Am Chem Soc* 128(11):3728–3736.
35. Babu CS, Lim C (1999) Theory of ionic hydration: Insights from molecular dynamics simulations and experiment. *J Phys Chem B* 103:7958–7968.
36. Pronk S, et al. (2013) GROMACS 4.5: A high-throughput and highly parallel open source molecular simulation toolkit. *Bioinformatics* 29(7):845–854.
37. Hess B, Bekker H, Berendsen HJC, Fraaije JGEM (1997) LINCS: A linear constraint solver for molecular simulations. *J Comput Chem* 18:1463–1472.
38. Parrinello M, Rahman A (1981) Polymorphic transitions in single crystals: A new molecular dynamics method. *J Appl Phys* 52:7182–7190.
39. Englander SW, Kallenbach NR (1983) Hydrogen exchange and structural dynamics of proteins and nucleic acids. *Q Rev Biophys* 16(4):521–655.
40. Bai Y, Milne JS, Mayne L, Englander SW (1993) Primary structure effects on peptide group hydrogen exchange. *Proteins* 17(1):75–86.
41. Vendruscolo M, Paci E, Dobson CM, Karplus M (2003) Rare fluctuations of native proteins sampled by equilibrium hydrogen exchange. *J Am Chem Soc* 125(51):15686–15687.
42. Best RB, Vendruscolo M (2006) Structural interpretation of hydrogen exchange protection factors in proteins: Characterization of the native state fluctuations of CI2. *Structure* 14(1):97–106.